Research Article Vol. 13, No. 4 / April 2026 / Optica 771

Turbulence-resilient macroscopic Fourier ptychography

Junhao Zhang,[1,2,3,4,5,†] Sheng Li,[6,7,†] Weilong Wei,[1,3,4,5] Bowen Wang,[6,7] Kaiyuan Yang,[1,2,3,4,5] Hongmei Wang,[8,9] Qiang Zhou,[2,10,11] Haotong Ma,[1,3,4,5] Ge Ren,[1,3,4,5] Chao Zuo,[6,7,12] and Zongliang Xie[1,3,4,5,13]

[1]Institute of Optics and Electronics, Chinese Academy of Sciences, Chengdu 610209, China
[2]University of Electronic Science and Technology of China (UESTC), Chengdu 610054, China
[3]State Key Laboratory of Optical Field Manipulation Science and Technology, Institute of Optics and Electronics, Chinese Academy of Sciences, Chengdu 610209, China
[4]Key Laboratory of Optical Engineering, Chinese Academy of Sciences, Chengdu 610209, China
[5]University of Chinese Academy of Sciences, Beijing 100049, China
[6]Smart Computational Imaging Laboratory (SCILab), School of Electronic and Optical Engineering, Nanjing University of Science and Technology, Nanjing, China
[7]Jiangsu Key Laboratory of Spectral Imaging & Intelligent Sense, Nanjing, China
[8]School of Science and Technology, Hong Kong Metropolitan University, Ho Man Tin, Hong Kong SAR Special Administrative Region of China, China
[9]Shanghai Golden Deep Technology Corporation, Shanghai 200135, China
[10]Institute of Fundamental and Frontier Sciences, University of Electronic Science and Technology of China, Chengdu 610054, China
[11]Research Center for Quantum Internet, Tianfu Jiangxi Laboratory, Chengdu 641419, China
[12]zuochao@njust.edu.cn
[13]xiezl@ioe.ac.cn
[†]These authors contributed equally to this work.

Received 2 February 2026; revised 16 March 2026; accepted 16 March 2026; published 10 April 2026

Fourier ptychography (FP) enables synthetic aperture imaging beyond the coherent diffraction limit of the imaging system, yet its extension to long-range scenarios remains fundamentally hindered by atmospheric turbulence. Turbulence introduces stochastic, time-varying wavefront distortions that violate both the deterministic pupil model and the coherent spectral overlapping required by FP, rendering conventional reconstruction strategies physically inconsistent. Here, we propose turbulence-resilient macroscopic Fourier ptychography (TRMFP), a unified computational framework that reformulates FP as a statistically consistent imaging process through random media. TRMFP integrates a speckle-interferometry-inspired preprocessing stage with a closed-loop ptychographic reconstruction. By exploiting ensemble statistics from multiple short-exposure measurements at each aperture position, TRMFP recovers turbulence-suppressed, diffraction-limited sub-aperture images, followed by joint optimization of the object and spatially varying wavefront aberrations under low-rank and total-variation constraints. Simulations and experiments validate the robustness of TRMFP across a wide range of turbulence strengths ($D/r_0 = 1.5$ to 7.5), achieving ∼2× resolution improvement in 1.5 m phase-screen experiments and ∼1.6× gain under 5 m dynamic turbulence over conventional FP. Without requiring additional hardware, wavefront sensors, or training data, TRMFP establishes a physically grounded and computationally efficient solution for super-resolution imaging through atmospheric turbulence, bridging the gap between Fourier ptychography and real-world long-range synthetic aperture imaging applications.

https://doi.org/10.1364/OPTICA.592286

1. INTRODUCTION

Spatial resolution of practical optical systems faces two fundamental limitations: aperture size and atmospheric turbulence. Aperture size governs the diffraction limit, as described by the Rayleigh criterion, restricting the minimum resolvable feature size with the angular resolution given by $1.22\lambda/D$, where λ is the center wavelength, and D denotes the size of the imaging aperture. Meanwhile, when the aperture size surpasses the atmospheric coherence diameter r_0, the system's angular resolution transitions from being aperture-limited to a turbulence-dominated regime. For example, atmospheric turbulence limits angular resolution to about 0.5–1 arcsec; consequently, a 4 m telescope has approximately the same resolving capabilities as a small 10 cm diameter tube [1]. These intertwined physical limitations hinder high-resolution imaging in scenarios ranging from ground-based astronomy to airborne surveillance.

Synthetic aperture (SA) imaging attempts to circumvent the diffraction barrier inherent to single-aperture systems [2,3] by

synthesizing a large aperture with multiple sub-apertures; the resolution is then determined by the synthetic aperture size, which can exceed that of a single aperture by orders of magnitude. However, traditional interferometric synthetic aperture (SA) techniques, while well-established in radio astronomy [4,5], where phase coherence can be precisely measured and maintained across long baselines, encounter difficulties when transposed to the optical regime. These challenges arise because direct optical detectors record only intensity, discarding the crucial phase information. An optical SA system must ensure the confocality (spatial overlap of focal volumes) and cophase alignment (phase synchronization) among sub-apertures [6–8], which necessitates ultrahigh-precision phase detection and dynamic posture control, hindering its widespread engineering applications.

Fourier ptychography (FP) has emerged as a promising computational SA technique [9,10]. It merges the principle of phase recovery and SA imaging, achieving sub-diffraction imaging without strict phase matching requirements. FP reconstructs high-resolution complex fields by iteratively stitching low-resolution images captured under varied illumination angles or different aperture locations. Since its first demonstration [9], FP has gained substantial research interest, finding significant applications in biomedical and pathological studies [10–18]. Efforts have also been directed toward extending FP principles to macroscopic scales for long-range imaging [19–28]. In 2014, Dong *et al.* [19] demonstrated that by replacing angle-varied illumination with aperture or camera scanning, FP can be extended to far-field imaging as macroscopic FP. Subsequent advancements by Holloway *et al.* [20] introduced a synthetic aperture visible imaging (SAVI) framework based on macroscopic FP, followed by a long-range reflective FP implementation demonstrating a six-fold resolution enhancement [21]. The recent work has focused on improving macroscopic FP's performance, including expanding the imaging field of view [22,23], reducing speckle noise [24], improving temporal resolution [25,26], correcting aberrations [27,28], and adapting the method for moving targets [29].

However, these advancements predominantly assume ideal, turbulence-free conditions, creating a significant gap between laboratory demonstrations and practical field deployment. Atmospheric turbulence disrupts imaging through spatiotemporal fluctuations in refractive index ($\Delta n(\boldsymbol{r}, t)$), governed by Kolmogorov's $k^{-5/3}$ power law (k is the wavenumber) [30,31]. Over long propagation paths, accumulated phase distortions ($\phi_{\text{turb}} = \frac{2\pi}{\lambda}\int \Delta n ds$) fragment the optical wavefront into speckle patterns and reduce the effective coherent aperture area to $\sim(D/r_0)^2$ isoplanatic patches governed by Fried's parameter r_0 [32,33]. For FP, which relies critically on coherent overlap between adjacent sub-aperture spectra for phase retrieval, this manifests as two fatal disruptions: (i) dynamic phase errors disrupt the phase consistency required for sub-aperture stitching, and (ii) each captured intensity becomes a turbulence-corrupted realization, violating the FP forward model. Since turbulence is a fast time-varying pupil error [34], existing FP aberration correction techniques (e.g., pupil function recovery [27] and phase diversity [28]) fail here as they are designed for static errors and lack the temporal resolution required for dynamic turbulence compensation. Not until the turbulence problem is effectively addressed could FP be applied in ground-based long-distance implementations.

In this work, we present a turbulence-resilient framework for long-range Fourier ptychography (FP), termed turbulence-resilient macroscopic Fourier ptychography (TRMFP), which integrates a speckle-interferometry-inspired turbulence correction [35,36] with ptychographic reconstruction in a unified computational pipeline. The main contributions of this work are three-fold: (i) We reformulate Fourier ptychography as a statistically consistent imaging problem through random media by introducing a speckle-interferometry-inspired preprocessing stage that recovers diffraction-limited sub-aperture images from multiple short-exposure turbulence-distorted measurements. (ii) We propose a joint reconstruction framework that simultaneously estimates the high-resolution object and spatially varying residual wavefront aberrations, regularized by physically motivated low-rank and total-variation constraints, enabling robust correction of dynamic turbulence effects. (iii) We demonstrate, for the first time to our knowledge, a fully FP-compatible solution for dynamic atmospheric turbulence without additional hardware, wavefront sensing, or training data, validated through comprehensive simulations and long-range experiments. This two-stage, closed-loop framework preserves the hardware simplicity of macroscopic FP while significantly extending its applicability to real-world long-range imaging scenarios.

In the following sections, we first introduce the theoretical foundation and algorithmic implementation of the proposed method. We then validate our method with numerical and experimental results. Finally, we summarize the results and discuss future directions.

2. METHOD

A. Imaging Model and Problem Formulation

In this work, we focus on atmospheric turbulence, which originates primarily from temperature-induced refractive-index fluctuations. Three important parameters govern the optical effects of atmospheric turbulence: the Fried parameter r_0, characterizing the transverse spatial coherence length; the atmospheric coherence time t_0, describing the temporal scale over which the wavefront remains correlated; and the isoplanatic angle θ_0, defining the angular region over which the point-spread function (PSF) can be considered approximately invariant. Detailed descriptions of these parameters are presented in Appendix A.

These parameters collectively define the boundaries of our study. The turbulence strength is quantified by the ratio D/r_0, here D is the aperture diameter. To freeze the turbulence dynamics, we employ short-exposure acquisitions, with exposure times shorter than t_0. Furthermore, we adopt an isoplanatic imaging model, under which the PSF is assumed to be spatially uniform across the field of view. This simplification allows us to treat the turbulence-induced blur as a position-invariant pupil function during the reconstruction.

With this turbulence model in place, the forward formation model is depicted in Fig. 1(a). The TRMFP system employs a coherent laser source and a projective lens to illuminate the target, with reflected light captured by a translating camera to acquire low-resolution (LR) images across multiple scanning positions. While sharing the core architecture of conventional macro-FP systems, TRMFP introduces a critical operation: at each scanning position, multiple short-exposure images are captured to sample turbulence-distorted realizations, as shown in Fig. 1(b). The exposure time should be shorter than the turbulence coherence time (typically <10 ms [37,38]) to "freeze" the atmospheric turbulence. Notably, this multi-frame acquisition strategy fundamentally

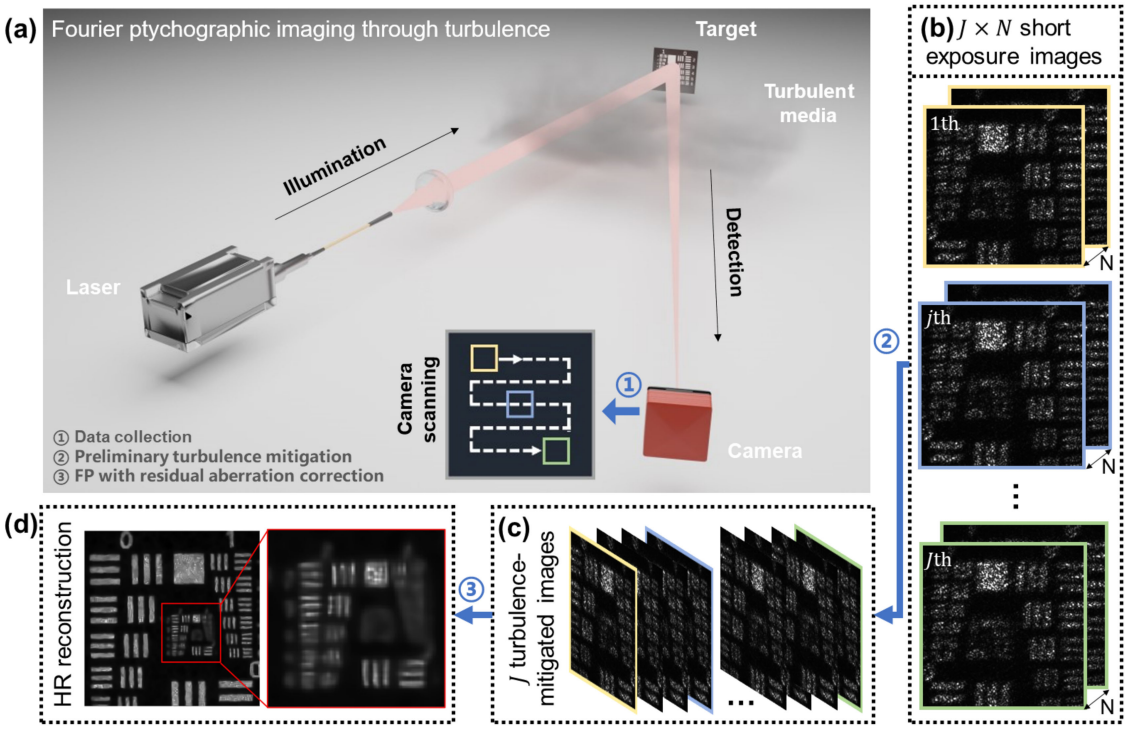

Fig. 1. Principle of turbulence-resilient macroscopic Fourier ptychography (TRMFP). (a) A distant object is illuminated with a coherent source; the reflected signal is captured by a camera through turbulent media. The camera then scans across the desired synthetic aperture. In each scanning location, N short-exposure random-distorted raw images are captured. (b) By translating the camera to J positions, a total of $J \times N$ images are captured. Preliminary turbulence mitigation is performed for raw images at each scanning location, then (c) the turbulence-suppressed data, which is composed of J recovered diffraction-limited images, is obtained. After computational reconstruction with residual-aberration correction and denoising, we finally obtain (d) the recovered high-resolution images.

differs from approaches like SAVI [21], where frame averaging aims to reduce read noise and increase dynamic range. In contrast, TRMFP's short-exposure sampling is specifically designed to capture independent turbulence realizations for subsequent processes that mitigate wavefront distortions. The image formation model can be summarized as

$$I_{n,j}(\boldsymbol{x}) \propto |\mathcal{F}\{\Omega(\boldsymbol{u}-\boldsymbol{u}_j)\cdot P_{n,j}(\boldsymbol{u})\}|^2, \tag{1}$$

where $\boldsymbol{x}$ and $\boldsymbol{u}$ denote the spatial and spatial-frequency coordinates, respectively, with $\boldsymbol{u}_j$ representing the relative frequency shift induced by the jth aperture position. The complex wavefield emanating from the object is described by $\Omega(\boldsymbol{u})$, and the pupil function is modeled as $P_{n,j}(\boldsymbol{u})$, which accounts for the nth unique turbulence distortion at jth aperture position. The Fourier transform operator is denoted by $\mathcal{F}\{\cdot\}$. The nth captured intensity image, corresponding to the jth aperture position, is expressed as $I_{n,j}(\boldsymbol{x})$, where the subscript n indexes sequential acquisitions under turbulence-distorted conditions at the same frequency spectrum location.

If we randomly select one short-exposure image as the measurement I_j^{meas} at each scanning position, the optimization problem can be formulated as

$$\min_{\Omega,\{P_j\}} \sum_j \left|\left||\mathcal{F}^{-1}[P_j\cdot\Omega]| - \sqrt{I_j^{\text{meas}}}\right|\right|_2^2. \tag{2}$$

This is a highly ill-posed problem. The number of unknowns (the object plus a distinct pupil for each scanning position) vastly exceeds the available intensity measurements. More critically, the wavefront perturbations induced by turbulence can vary dramatically across different scan positions, substantially increasing the difficulty of inversion. Conventional FP can only correct static pupil errors and is therefore unlikely to be suitable for real-time correction. Phase diversity [28] represents a promising approach, but it introduces additional system complexity.

In this work, we adopt a two-stage approach, as shown in Figs. 1(b)–1(d). The first-stage processes the short-exposure stack at each scan position [Fig. 1(b)] to obtain a turbulence-suppressed, diffraction-limited sub-aperture image [Fig. 1(c)], effectively reducing the magnitude of pupil variations and providing a well-conditioned starting point for further refinement. In the second stage, we propose a joint optimization that simultaneously recovers the spatially varying pupil functions and high-resolution target [Fig. 1(d)]. This is achieved through an iterative scheme with embedded orthogonal-mode and total-variation constraints, which corrects residual aberrations within the reconstruction loop.

B. Preliminary Turbulence Mitigation

The preliminary turbulence mitigation step is founded on a principle derived from speckle interferometry [35,39]: a diffraction-limited sub-image can be computationally recovered from an ensemble of short-exposure, turbulence-distorted captures by leveraging their inherent statistical information. Here, the short-exposure condition ensures that each frame freezes a distinct turbulence realization while the object's intrinsic speckle pattern remains static; thus, ensemble-averaging operates on the random turbulent point-spread functions, preserving the object's

speckle statistics for subsequent recovery. To this end, TRMFP introduces a novel preprocessing step that corrects atmospheric turbulence in FP's raw sub-images, enabling robust reconstruction under adverse conditions.

The recovery of diffraction-limited sub-images proceeds in two distinct stages: (1) estimation of the Fourier amplitude, and (2) retrieval of the Fourier phase. A fundamental consideration is that while speckle interferometry typically relies on an incoherent imaging model, FP is inherently based on a coherent model. To reconcile this discrepancy, we formulate the image degradation process as a convolution of the original sharp image $I(\boldsymbol{x})$ with an unknown, random blur kernel $h_n(\boldsymbol{x})$, expressed as

$$I_n(\boldsymbol{x}) = I(\boldsymbol{x}) \otimes h_n(\boldsymbol{x}), \tag{3}$$

and

$$\tilde{I}_n(\boldsymbol{u}) = \tilde{I}(\boldsymbol{u}) \cdot \tilde{H}_n(\boldsymbol{u}), \tag{4}$$

where $\otimes$ denotes the convolution operator, $I_n(\boldsymbol{x})$ denotes the nth distorted image, and Eq. (4) is the Fourier transform of Eq. (3). It is important to emphasize that this reformulation does not imply a loss of coherence in the physical imaging system. Rather, it serves as a statistical surrogate model that enables robust recovery of the object's Fourier amplitude under random phase perturbations induced by atmospheric turbulence. The established image degradation model is now formally consistent with the incoherent imaging model. We aim to recover the original sharp image $I(\boldsymbol{x})$ from the distorted image $I_n(\boldsymbol{x})$, which is equivalent to recovering its Fourier spectrum $\tilde{I}(\boldsymbol{u})$. Short-exposure images retain high-spatial-frequency information up to the diffraction limit, despite turbulence-induced phase corruption. By ensemble-averaging the power spectra $<|\tilde{I}_n(\boldsymbol{u})|^2>$ of multiple distorted images, the original image's Fourier amplitude $|\tilde{I}(\boldsymbol{u})|^2$ can be retrieved as

$$<|\tilde{I}_n(\boldsymbol{u})|^2> = |\tilde{I}(\boldsymbol{u})|^2 \cdot <|\tilde{H}_n(\boldsymbol{u})|^2>, \tag{5}$$

where $<|\tilde{H}_n(\boldsymbol{u})|^2>$ is the energy spectrum of the turbulent point-spread function (PSF), which describes how the spectral components of the image are transmitted by the atmosphere and the imaging system. At every moment, this function is unknown, but its time-averaged value can be determined as non-zero up to the diffraction limit under stationary turbulence conditions.

Merely obtaining the Fourier amplitude is insufficient for sub-image reconstruction. The complete recovery of Fourier phase information is fundamentally indispensable. Here, we propose to use a FP shift-and-add approach to estimate the Fourier phase. To start with, the nth distorted kernel $h_n(\boldsymbol{x})$ that is randomly generated by turbulence can be represented as

$$h_n(\boldsymbol{x}) = h_{\text{ideal}}(\boldsymbol{x}) \otimes R_n(\boldsymbol{x}), \tag{6}$$

where $h_{\text{ideal}}(\boldsymbol{x})$ is the ideal diffraction-limited PSF, and $R_n(\boldsymbol{x})$ is the nth instantaneous random position and weights caused by random distortion. When simply ensemble average $h_n(\boldsymbol{x})$, only a constant featureless blur is obtained, because

$$\begin{aligned} <h_n(\boldsymbol{x})> &= h_{\text{ideal}}(\boldsymbol{x}) \otimes <R_n(\boldsymbol{x})> \\ &= h_{\text{ideal}}(\boldsymbol{x}) \otimes \text{constant background} \\ &= \text{constant background}. \end{aligned} \tag{7}$$

But if we perform coherent averaging of $h_n(\boldsymbol{x})$ by first shift-correcting it to make its maximum value at the origin, and then ensemble-averaging the shift-corrected $h_{n,\text{corr}}(\boldsymbol{x})$, a different outcome will occur:

$$\begin{aligned} &<h_{n,\text{corr}}(\boldsymbol{x})> \\ &= h_{\text{ideal}}(\boldsymbol{x}) \otimes <R_{n,\text{corr}}(\boldsymbol{x})> \\ &= h_{\text{ideal}}(\boldsymbol{x}) \otimes <a'_n \delta(\boldsymbol{x}) + R'_{n,\text{corr}}(\boldsymbol{x})> \\ &= h_{\text{ideal}}(\boldsymbol{x}) \otimes <a'_n \delta(\boldsymbol{x})> + h_{\text{ideal}}(\boldsymbol{x}) \otimes <R'_{n,\text{corr}}(\boldsymbol{x})> \\ &= h_{\text{ideal}}(\boldsymbol{x}) + \text{constant background}, \end{aligned} \tag{8}$$

where $a'_n \delta(\boldsymbol{x})$ are maximum values at the origin, and $R'_{n,\text{corr}}(\boldsymbol{x})$ are the remaining random terms. One can see that by simply shift-correcting $h_n(\boldsymbol{x})$ before averaging, the ideal PSF $h_{\text{ideal}}(\boldsymbol{x})$ is preserved. Since both $h_{\text{ideal}}(\boldsymbol{x})$ and the constant background are real-valued and symmetric, the Fourier transform of $<h_{n,\text{corr}}(\boldsymbol{x})>$ is purely real, resulting in a zero-phase Fourier spectrum. Moreover, the Fourier amplitude of $<h_{n,\text{corr}}(\boldsymbol{x})>$ has nonzero values up to the diffraction limit. Therefore, combining with Eq. (3), the Fourier phase of an object can be directly retrieved through simply coherent averaging randomly distorted images:

$$\phi(\boldsymbol{u}) = \angle \mathcal{F}\{I_{\text{avg}}(\boldsymbol{x})\}, \tag{9}$$

where $\phi(\boldsymbol{u})$ is the retrieved phase, and $I_{\text{avg}}(\boldsymbol{x})$ is the averaging of the shift-corrected $\{I_{n,\text{corr}}(x)\}$. Combining Eqs. (8) and (9) yields the turbulence-corrected image:

$$I^{\text{post}}(\boldsymbol{x}) = \mathcal{F}^{-1}\{<|\tilde{I}(\boldsymbol{u})|> \cdot \exp(i\phi(\boldsymbol{u}))\}, \tag{10}$$

where $\mathcal{F}^{-1}\{\cdot\}$ denotes the inverse Fourier transform. Notably, the pivotal step enabling turbulence mitigation for FP is the recovery of the Fourier phase $\phi(\boldsymbol{u})$ via Eq. (9). This retrieved phase, combined with the Fourier amplitude, allows the reconstruction of the diffraction-limited image $I^{\text{post}}(\boldsymbol{x})$ for each sub-aperture j. We summarize the whole process of preliminary turbulence mitigation in Algorithm 1. Following this, the turbulence-suppressed images enter a refinement process, which is detailed in Section 2.C.

Notably, the number of frames N per scanning position is critical for preliminary turbulence mitigation. Larger N improves reconstruction fidelity but increases acquisition time and computational load. We find that $N = 20$ provides a practical balance between performance and efficiency under moderate turbulence, while $N = 50$ is recommended for stronger turbulence to ensure robust recovery. Accordingly, we adopt $N = 50$ in simulations and $N = 20$ in experiments throughout this work.

C. Residual Aberration Correction

Under conditions of strong turbulence or with an insufficient number of short-exposure frames, the initial processing stage may not fully eliminate all wavefront distortions, leaving residual aberrations in the preliminary sub-aperture images. To achieve a final diffraction-limited reconstruction, TRMFP introduces a subsequent correction mechanism specifically designed to address these residual phase errors.

Building upon the pre-corrected data, the residual aberrations, though still exhibiting a spatially varying nature, are significantly

Algorithm 1. Preliminary Turbulence Mitigation

Input: $J \times N$ distorted raw images $I_{n,j}(\boldsymbol{x})$, a selected reference image $I_0(\boldsymbol{x})$
Output: J turbulence-suppressed images $I_j^{\text{post}}(\boldsymbol{x})$
for j = 1 : J **do** ▷ different scanning positions
  $<|\tilde{I}_j(\boldsymbol{u})|> = \sqrt{\frac{1}{N}\sum |\tilde{I}_{n,j}(\boldsymbol{u})|^2}$ ▷ Extract Fourier amplitude
  for n = 1 : N **do** ▷ short exposure measurement
    $\Delta x \leftarrow I_0(\boldsymbol{x}) \star I_{n,j}(\boldsymbol{x})$ ▷ Cross-correlation
    $I_{n,\text{corr}}(\boldsymbol{x}) = I_{n,j}(\boldsymbol{x} + \Delta\boldsymbol{x})$ ▷ Shift correction
  $I_{\text{avg}}(\boldsymbol{x}) = \frac{1}{N}\sum I_{n,\text{corr}}(\boldsymbol{x})$ ▷ Ensemble average
  $\phi_j(\boldsymbol{u}) = \angle\mathcal{F}\{I_{\text{avg}}(\boldsymbol{x})\}$ ▷ Extract Fourier phase
  $I_j^{\text{post}}(\boldsymbol{x}) = \mathcal{F}^{-1}\{<|\tilde{I}_j(\boldsymbol{u})|> \cdot \exp(i\phi_j(\boldsymbol{u}))\}$ ▷ Image reconstruction

reduced in magnitude compared to the original turbulent distortions. These residual aberrations can be modeled by a set of spatially varying pupil functions $\{P_j\}$. This prior stabilization effectively confines the solution space and lowers the ill-posedness of the subsequent joint estimation, thereby opening the possibility for stable and efficient joint reconstruction of the object spectrum $\Omega(\boldsymbol{u})$ and the pupil functions $\{P_j\}$. Here, we reformulate the optimization problem as

$$\min_{\Omega,\{P_j\}} \sum_j \left\| |\mathcal{F}^{-1}[P_j \cdot \Omega]| - \sqrt{I_j^{\text{post}}} \right\|_2^2 + \lambda_{\text{support}} \sum_j R_{\text{support}}(P_j) + \lambda_{\text{TV}} \sum_j R_{\text{TV}}(P_j) \times \text{s.t.} \quad \text{rank}(\mathbf{P}) \le R, \tag{11}$$

where $\mathbf{P} = [P_1, \ldots, P_J]$ stacks all pupil vectors, the first term is the data fidelity term, the second and third terms are the pupil support and pupil total-variation (TV) regularizer, respectively. The parameters λ_{support} and λ_{TV} balance the strength of the support and total-variation terms. The rank constraint restricts the pupil variations to a subspace of dimension $R \ll J$. Physically, the imposed low-rank constraint reflects the fact that residual turbulence-induced aberrations across different scanning positions are highly correlated and dominated by a limited number of common modes, rather than being independent random distortions.

To solve this problem, we propose an alternating projection algorithm, which extends the embedded pupil function recovery (EPRY) approach [40] by integrating proximal operations for the physical constraints and a global low-rank projection step. The procedure can be summarized in two nested loops.

In the inner loop, we perform a sequential scan over all measurement positions. For the jth position, we retrieve the corresponding pupil estimate P_j from the current pupil stack. The pupil is then regularized via a total-variation proximal operator to promote spatial smoothness:

$$\tilde{P}_j = \text{prox}_{\lambda R_{\text{TV}}}(P_j), \tag{12}$$

which is implemented using the fast gradient projection algorithm [41].

A binary support mask CTF defined by the system aperture (one inside the pupil support, zero outside), is subsequently applied to enforce the physical aperture boundary:

$$\hat{P}_j = \tilde{P}_j \cdot \text{CTF}. \tag{13}$$

Using the regularized pupil $\hat{P}_j$, we update the object spectrum and the pupil simultaneously using the EPRY approach. The update rules follow the standard gradient descent scheme on the data fidelity term, yielding new estimates for both Ω and P_j. Notably, the support constraint is enforced again on the newly updated pupil to ensure physical consistency before it is stored back into the stack.

After a complete pass through all scanning positions, in the outer loop, the entire set of estimated pupils is organized into the matrix $\mathbf{P} = [P_1, \ldots, P_J]$. This matrix is projected onto the rank-R matrix via truncated singular value decomposition (SVD):

$$\mathbf{P} \leftarrow \Pi_{\text{rank}\le R}(\mathbf{P}) = U_{:,:,R}\,\Sigma_{:,:,R}\,V^*_{:,:,R}, \tag{14}$$

where the U, Σ, and V are the factors of the SVD of $\mathbf{P}$. This step enforces that all pupil estimates share a low-dimensional subspace, thereby capturing the correlated nature of the residual turbulence aberrations across scanning positions [18,42,43]. Additionally, the rank R is selected based on the singular value spectrum of the pupil matrix. We retain the top singular components capturing the dominant energy (e.g., 95% of the total). Across our experiments, we find that $R = 5$ consistently yields stable reconstructions when the first-stage mitigation is effective. For stronger turbulence where first-stage processing fails, reconstruction quality is limited by the preprocessing stage rather than the choice of R. The whole recovery process is summarized in Algorithm 2.

3. SIMULATIONS

In this section, we use simulation to benchmark our method and characterize its performance. Images of 256 × 256 pixels are served as the object, the wavelength is set to 632 nm, the simulated pixel size is 2.4 μm, and the F-number is set to 8, resulting in a pupil diameter of 60 pixels. A synthetic aperture is formed by simulating a 11 × 11 grid of camera positions with a step size of 12 pixels, which corresponds to an overlap ratio of approximately 87.26% in the Fourier domain between adjacent measurements. This relatively high overlap was chosen to ensure stable phase retrieval, as lower overlap reduces spectral redundancy between adjacent sub-apertures, weakening phase constraints and potentially introducing artifacts. Previous studies [20,21,40] suggest that overlap above 65% is generally sufficient for stable phase retrieval in conventional FP, and we anticipate a similar trend for TRMFP, with robust performance above this threshold and graceful degradation as overlap decreases further. At each position, 50 turbulence-distorted short-exposure images are generated.

The turbulence-distorted images are simulated based on the classical phase-screen method with Zernike polynomials (see Appendix B) [30,31]. Notably, the degree of turbulence is quantified using the parameter D/r_0 [32]. Resolving power is limited by the imaging system itself only when $D < r_0$, in other cases it is limited by the turbulence. Therefore, the larger the value of D/r_0, the more severe the turbulence and the lower the resolution.

A. Comparison of Different Methods

To verify the effectiveness of TRMFP, we conducted simulations to compare the proposed TRMFP with conventional FP and FP with simple averaging at a fixed turbulence level ($D/r_0 = 5$). For

Algorithm 2. Fourier Ptychographic Reconstruction with Orthogonal Pupil Constraints via Alternating Projections

Input: The turbulence-suppressed images $I_j^{\text{post}}(\boldsymbol{x}),\ j = 1, \ldots, J$
Output: The object spectrum $\Omega(\boldsymbol{u})$ and the spatially varying pupil functions $\{P_j(\boldsymbol{u})\}$

for k = 1 : K **do** ▷ iterations
  for j = 1 : J **do** ▷ different scanning positions
    $P_j(\boldsymbol{u}) = \mathbf{P}^k(:, :, j)$ ▷ Extract j-th pupil
    $\hat{P}_j(\boldsymbol{u}) = \text{prox}_{\lambda R_{\text{TV}}}(P_j(\boldsymbol{u})) \cdot \text{CTF}$ ▷ TV regularization and support constraint
    $\Psi_j(\boldsymbol{u}) = \Omega_j^k(\boldsymbol{u} - \boldsymbol{u}_j) \cdot \hat{P}_j(\boldsymbol{u})$
    $\psi_j(\boldsymbol{x}) = \mathcal{F}^{-1}\{\Psi_j(\boldsymbol{u})\}$ ▷ Forward propagation
    $\psi_j^{\text{new}}(\boldsymbol{x}) = \sqrt{I_j^{\text{post}}(\boldsymbol{x})} \cdot \exp\{i \cdot \text{angle}[\psi_j(\boldsymbol{x})]\}$ ▷ Intensity constraint
    $\Psi_j^{\text{new}}(\boldsymbol{u}) = \mathcal{F}\{\psi_j^{\text{new}}(\boldsymbol{x})\}$
    $\Omega_j^{k+1}(\boldsymbol{u} - \boldsymbol{u}_j) = \Omega_j^k(\boldsymbol{u} - \boldsymbol{u}_j) + \frac{\text{conj}(\hat{P}_j(\boldsymbol{u}))}{\max^2(|\hat{P}_j(\boldsymbol{u})|)} \times [\Psi_j^{\text{new}}(\boldsymbol{u}) - \Psi_j(\boldsymbol{u})]$ ▷ Update object spectrum
    $\hat{P}_j^{\text{new}}(\boldsymbol{u}) = \hat{P}_j(\boldsymbol{u}) + \frac{\text{conj}(\Omega_j^k(\boldsymbol{u}-\boldsymbol{u}_j))}{\max^2(\Omega_j^k(\boldsymbol{u}-\boldsymbol{u}_j))} \times [\Psi_j^{\text{new}}(\boldsymbol{u}) - \Psi_j(\boldsymbol{u})]$ ▷ Update j-th pupil
    $\hat{P}_j^{\text{new}}(\boldsymbol{u}) = \hat{P}_j^{\text{new}}(\boldsymbol{u}) \cdot \text{CTF}$ ▷ Support constraint
    $\mathbf{P}^{k+1}(:, :, j) = \hat{P}_j^{\text{new}}(\boldsymbol{u})$ ▷ Put into pupil stack
  $\mathbf{P}^{k+1} \leftarrow \Pi_{\text{rank} \le R}(\mathbf{P}^{k+1}) = U_{:,:,R} \Sigma_{:,:,R} V^*_{:,:,R}$ ▷ SVD low-rank projection

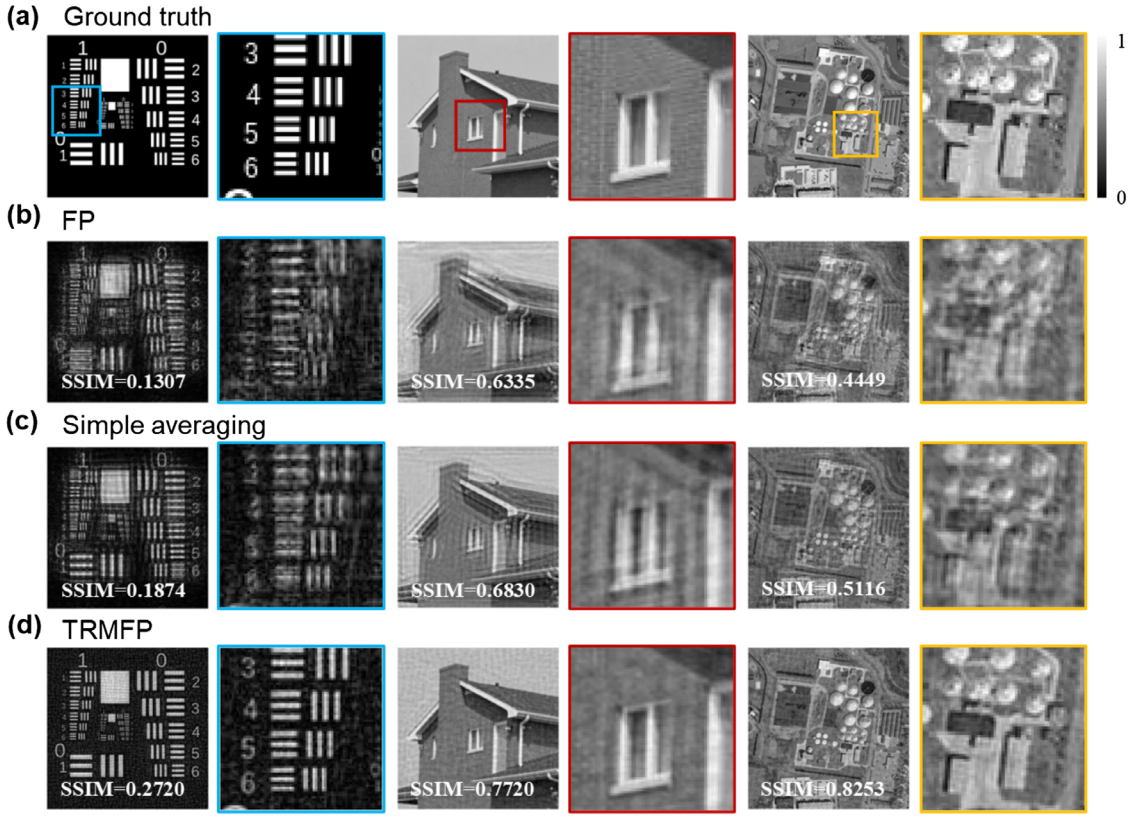

Fig. 2. Comparison of different methods for various test images (from left to right: *USAF target, House, Storage tanks*). (a) The ground -truth. (b) The reconstructions using conventional FP. (c) The reconstructions using FP with simply averaged data. (d) The reconstructions using TRMFP.

TRMFP reconstruction of the dataset, an initial step involves performing preliminary turbulence mitigation on the 50 distorted images at each measurement position to obtain a turbulence-corrected intensity estimation. This pre-corrected dataset is then reconstructed using our proposed FP algorithm with residual-aberration correction. For conventional FP, a single distorted image is randomly chosen from each position to form the basis of FP reconstruction. For simple averaging, all the distorted images from each position are averaged to obtain an equivalent long-exposure image. All three methods employ 100 iterations of their respective FP reconstruction routines, and their results are quantitatively evaluated with the structure similarity index (SSIM, see Appendix C) by comparing the reconstructed images with respect to the ground -truth.

Figure 2 presents a comparative analysis of the reconstruction results across various test images. Conventional FP, with low SSIM scores (0.1307, 0.6335, and 0.4449), yields results severely degraded by turbulence, exhibiting significant artifacts and a loss of fine details. The simple averaging approach (SSIM: 0.1874, 0.6830, and 0.5116) also fails to effectively address these issues, as

its inherent long-exposure equivalence suppresses high-frequency information. Conversely, TRMFP achieves substantially superior performance, with high SSIM values (0.2720, 0.7720, and 0.8253) and visually enhanced sharpness and detail. These results prove that neither conventional FP nor simple averaging can overcome turbulence-induced degradation, whereas TRMFP effectively restores high-resolution information under strong turbulence.

B. Performance under Various Turbulence Intensities

To test the boundaries of our method, we evaluated the performance of TRMFP under different turbulence intensities. We simulated 14 different turbulence levels by adjusting the values of D/r_0 from 3.5 to 10 at intervals of 0.5 and presented visualization results for four of them, as shown in Fig. 3. Again, to demonstrate TRMFP's superiority, the results of conventional FP are compared.

The performance comparison under varying turbulence intensities is summarized in Figs. 3(a) and 3(c). Under mild turbulence ($D/r_0 = 3.5$), both methods yield reasonable reconstructions, with TRMFP (SSIM = 0.8684) already outperforming conventional FP (SSIM = 0.7677). As turbulence intensifies to $D/r_0 = 5$, FP shows significant degradation (SSIM = 0.5460), whereas TRMFP maintains high fidelity (SSIM = 0.7880). Under strong turbulence ($D/r_0 = 7.5$), FP reconstructions become severely blurred (SSIM = 0.3734), while TRMFP continues to deliver usable results (SSIM = 0.6630). Even in extreme turbulence ($D/r_0 = 10$), TRMFP retains discernible structural details and an SSIM of 0.4586, demonstrating consistent resilience. The overall SSIM trends across all turbulence levels, shown in Figs. 3(b) and 3(d), confirm the clear and sustained superiority of TRMFP.

C. Robustness to Optically Rough Objects

Since real-world objects often scatter incident light in random directions because of surface roughness, it is essential to examine our method for optically rough objects. The rough objects are simulated by adding random phase terms to the original objects. Here, we use the USAF resolution target as the object's amplitude, while its phase is randomized between $-\pi$ to π. The results of TRMFP and conventional FP for the rough object under different turbulence conditions are shown in Fig. 4, where we quantify the results with the Pearson correlation coefficient (PCC; see Appendix C).

The reconstruction results for both FP and TRMFP on optically rough objects are presented in Figs. 4(a)–4(d). As evident from the images, the reconstruction quality is compromised not only by atmospheric turbulence but also by significant speckle noise arising from surface roughness. To address this combined degradation, we incorporate a speckle denoising step [24] into our processing pipeline. The denoised results, shown in Figs. 4(b) and 4(d), reveal a stark contrast in performance as turbulence intensity increases. While conventional FP reconstructions become severely blurred under stronger turbulence, TRMFP maintains remarkable resilience to turbulence-induced degradation. Quantitatively, under mild turbulence conditions ($D/r_0 = 1.5$), both methods achieve high-fidelity reconstructions with PCC values of 0.8923 (FP) and 0.9311 (TRMFP). As turbulence intensifies, FP performance degrades substantially (PCC = 0.7878), whereas TRMFP maintains excellent fidelity (PCC = 0.9026). Under extreme turbulence conditions ($D/r_0 = 5$ and $D/r_0 = 7.5$), FP results become completely blurred with PCC values dropping dramatically to 0.6654 ($D/r_0 = 5$) and 0.5701 ($D/r_0 = 7.5$). In contrast, TRMFP continues to resolve critical features while maintaining substantially higher PCC values of 0.8857 ($D/r_0 = 5$) and 0.8334 ($D/r_0 = 7.5$).

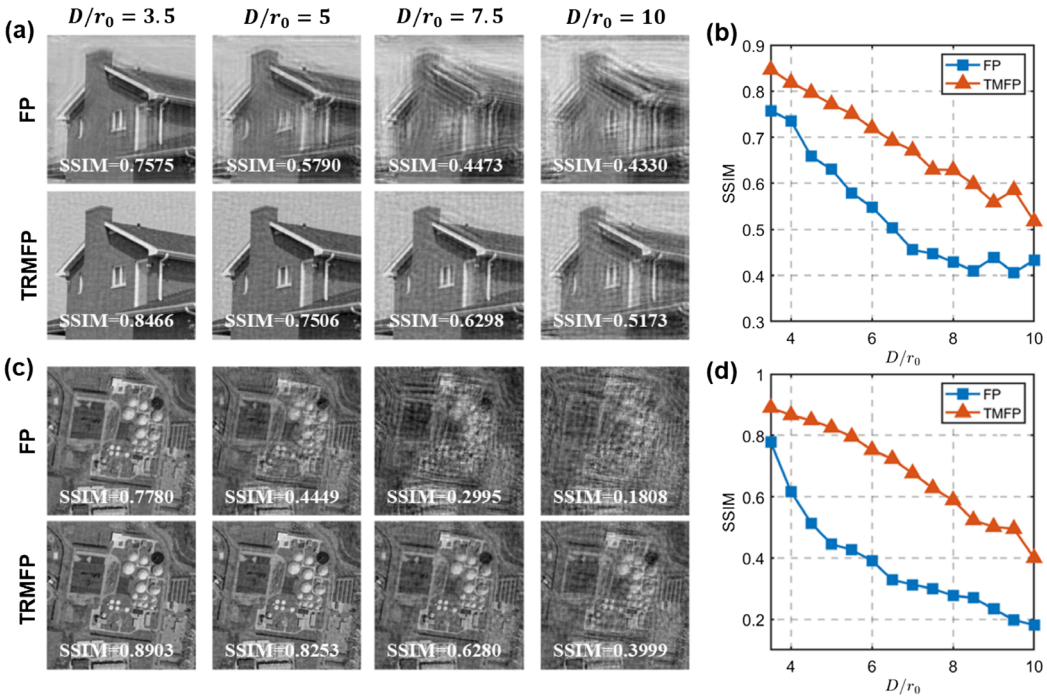

Fig. 3. Comparison of the performance of FP and TRMFP under various turbulence intensities. (a) Representative visual results of the *House* image. Columns: turbulence regimes (left to right: $D/r_0 = 3.5$, $D/r_0 = 5$, and $D/r_0 = 10$). (b) The SSIM values of FP and TRMFP results for the *House* image against the turbulence intensity. (c) Representative visual results of the *Storage tanks* image. (d) The SSIM values of FP and TRMFP results for the *Storage tanks* image against the turbulence intensity.

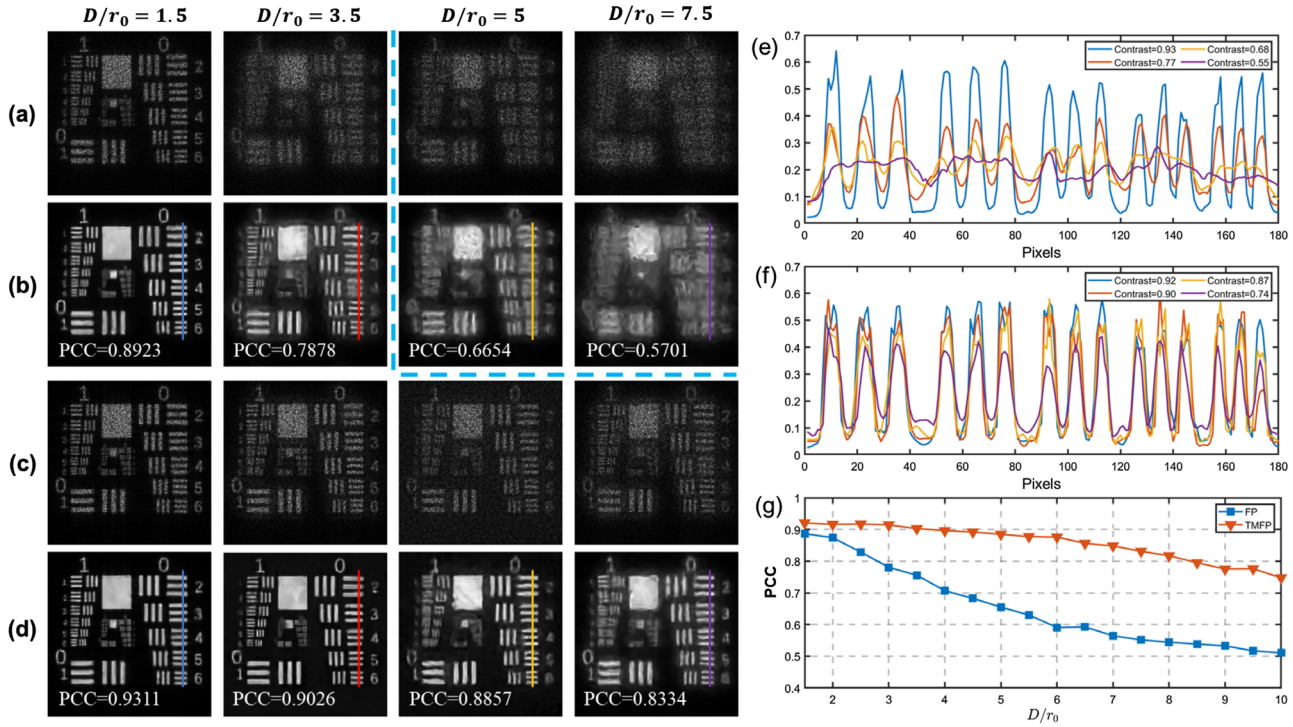

Fig. 4. Quantitative analysis of the robustness of our method to optically rough objects. (a) FP reconstructions without denoising. (b) FP reconstructions with denoising. (c) TRMFP without denoising. (d) TRMFP with denoising. (e) Quantitative comparison of the intensity profile along the indicated line traces in (b). (f) Quantitative comparison of the intensity profile along the indicated line traces in (d). (g) The PCC values of FP and TRMFP results against the turbulence intensity.

The superiority of TRMFP is also underscored by quantitative analysis of line traces across bar groups in reconstructed images, particularly through contrast metric evaluation. The contrast metric C is mathematically defined as

$$C = \frac{W - B}{W + B}, \tag{15}$$

where W and B represent the mean intensity values of white and black bars, respectively, extracted from the line trace profiles. As demonstrated in Figs. 4(e) and 4(f), the FP method exhibits contrast values of 0.93, 0.77, 0.68, and 0.55 under increasing turbulence conditions, while TRMFP maintains significantly higher contrasts of 0.92, 0.90, 0.87, and 0.74. This trend confirms that TRMFP preserves superior contrast stability across varying turbulence levels.

We further evaluate the results of both FP and TRMFP under a broad range of turbulence intensities ($D/r_0 = 1.5$ to 10, with 0.5 increments). As presented in Fig. 4(g), conventional FP demonstrates dramatic performance degradation beyond $D/r_0 = 2$, with PCC values plummeting rapidly. In contrast, TRMFP exhibits robust performance, maintaining PCC > 0.85 even at $D/r_0 < 7.5$. Collectively, these results demonstrate that TRMFP retains remarkable effectiveness for reconstructing optically rough objects under challenging turbulent conditions.

D. Validation of Residual Aberration Correction

In this section, we focus on evaluating the effectiveness of the proposed residual-aberration correction (RAC) algorithm independently. The residual wavefront errors are simulated using the same phase-screen model based on Zernike polynomials as employed for turbulence generation. It is crucial to note that, since we are modeling the scenario after preliminary turbulence correction, each scanning position corresponds to a single sub-aperture image degraded by these residual aberrations, rather than a stack of short-exposure frames. To this end, we design two targeted numerical experiments to validate the algorithm's performance and illustrate its practical bounds.

The first set compares the reconstruction performance under moderate residual aberrations (characterized by $D/r_0 = 3$). We contrast the results of conventional FP reconstruction (which assumes a static pupil) with those of RAC that jointly estimates the object and the spatially varying pupils. As shown in Fig. 5(a1), the significant improvement in reconstruction fidelity achieved by RAC clearly demonstrates its effectiveness.

The second set examines the performance dependence on the strength of residual aberrations. We present pupil reconstruction results for both moderate ($D/r_0 = 3$) and strong ($D/r_0 = 5$) residual errors using our correction algorithm. As shown in Figs. 5(b)–5(d), the comparison reveals that while the method performs robustly for moderate aberrations [Figs. 5(c1)–5(c3)], its effectiveness diminishes when the residual errors become too severe [Figs. 5(d1)–5(d3)]. This indicates that the proposed RAC achieves stable convergence only when the aberrations remain within a moderate range. The inherent limitation highlights the necessity of a preliminary turbulence-correction stage, which reduces strong turbulence to a level tractable for the subsequent aberration correction. The effectiveness of this two-stage strategy is confirmed again in Fig. 5(a2), where the full TRMFP pipeline delivers substantially superior reconstruction quality even under strong turbulence.

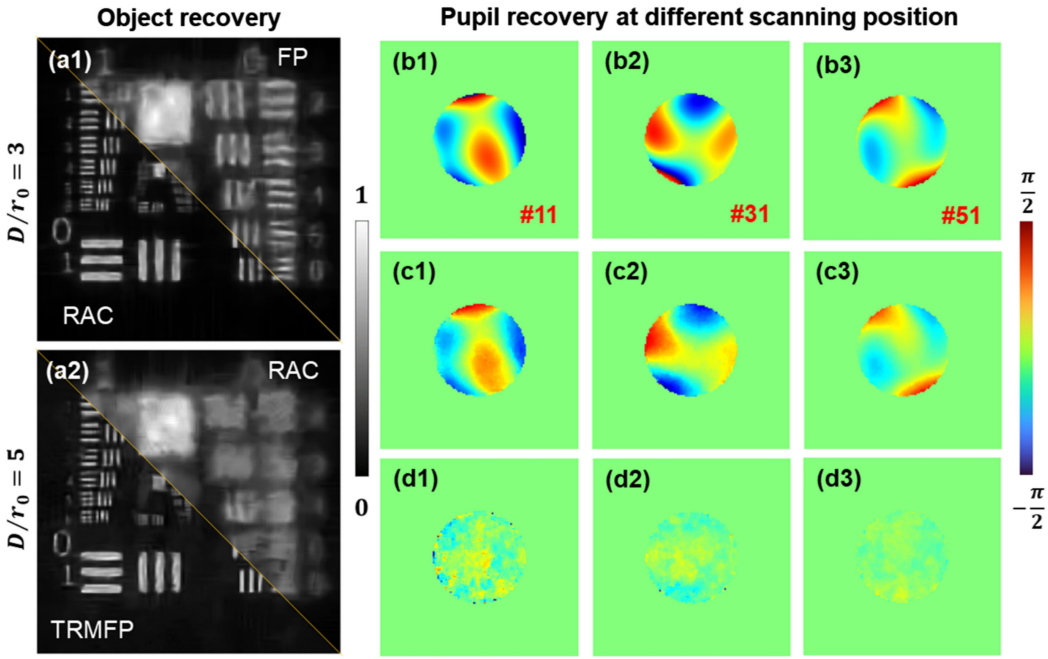

Fig. 5. (a1) The reconstructed object intensity with regular FP and our proposed residual-aberration correction (RAC) algorithm under moderate turbulence. (a2) The reconstructed object intensity with RAC and the full TRMFP method under strong turbulence. (b1)–(b3) Ground -truth of pupil at different scanning positions. (c1)–(c3) Pupil recovery at different scanning positions under moderated residual phase errors. (d1)–(d3) Pupil recovery at different scanning positions under strong residual phase errors.

4. EXPERIMENTS

A. Validation with Phase Screens

We conduct a proof-of-concept experiment to demonstrate the performance of the proposed method using phase screens. The experimental setup is shown in Fig. 6(a), and Table 1 reports the details of the experimental setup, where we employ a 639 nm laser source coupled to a single-mode fiber and collimated through a plano-convex lens (L1, focal length: 200 mm) to produce the illumination beam. The target is positioned 1.5 m away from the detection system. In the detection arm, a rotatable phase screen is placed in front of the camera to generate random turbulence distortion. A linear polarizer filters noninterference background light. Light from the target is collected using a photographic lens (L2, focal length: 50 mm, $f/8$ aperture) and detected by a monochrome camera (Imaging source, 2.4 μm pixel pitch). Two motorized stages are used to raster-scan the camera to different x–y positions with a step size of 1.5 mm, resulting in 85% Fourier domain overlap between adjacent positions. We note that the cross-correlation step in TRMFP's preprocessing provides inherent image registration, compensating for small positioning inaccuracies or stage jitter, and any residual errors can be absorbed into the per-position pupil estimation during joint optimization. At each scanning position, the phase screen is rotated to multiple angles to capture degraded images under different turbulence disturbances. Notably, the phase screen is placed solely in the detection arm, which means that we only consider the distortion on the reflection wavefront. This is reasonable because the effect of turbulence distortion on the illumination wavefront is limited as it can be overwhelmed by the random phase of rough objects.

For the experiments with phase screens, an exposure time of 80 ms is used for each measurement. Since the phase screen remains stationary during this exposure, the captured image represents a single, frozen instance of the turbulence distortion. This condition differs from real atmospheric turbulence, where exposure times must be shorter than the coherence time to freeze the wavefront. The static-screen setup thus provides a controlled, deterministic point-spread function for algorithm validation while simplifying the optical implementation.

In the first experiment, we use a USAF resolution test chart as the target (attached to a piece of paper to simulate scattering), as shown in Fig. 6(b). The camera is raster-scanned across a 11×11 grid, synthesizing an effective aperture of 21.35 mm, which is about 3.4× larger than the single aperture (6.25 mm). In each scanning position, the phase screen is rotated manually, and 20 distorted images are recorded, resulting in a dataset containing a total of 2420 turbulence-degraded images (11×11 positions $\times 20$ turbulence realizations. For benchmarking purposes, a turbulence-free dataset is acquired by removing the phase screen while ensuring identical scanning parameters and illumination conditions.

Figure 6(b) compares the sub-aperture raw image and the reconstruction results under three distinct conditions. The first one is the magnified region of the sub-aperture raw image, which is completely blurry. The last one is the reconstruction result of the turbulence-free dataset, from which we can see the maximum resolvable line pair is Group 2 Element 4, corresponding to an angular resolution of 5.89×10^{-5} rad. For a coherent imaging system operating under speckle conditions, the theoretical Rayleigh resolution limit is given by $R = 1.6\lambda/D$ [24]. Substituting the wavelength $\lambda = 639$ nm and the synthetic aperture size $D = 21.35$ mm, the calculated theoretical angular resolution is 4.79×10^{-5} rad, which aligns with the experimentally measured value. The second one is the FP reconstruction obtained from a single turbulence-corrupted image per scanning position. Turbulence-induced distortions severely degrade the imaging performance, reducing the maximum resolvable feature from

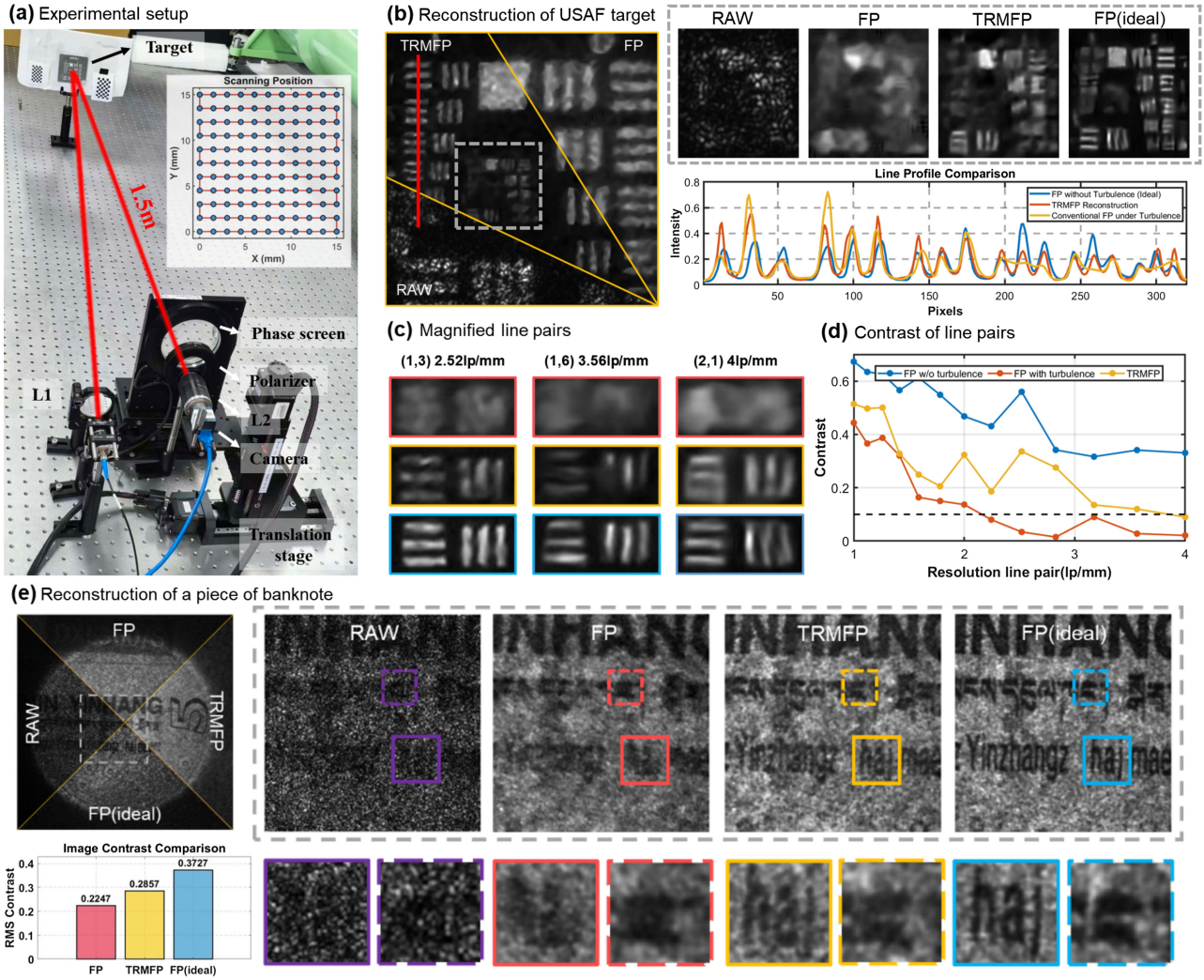

Fig. 6. TRMFP validation using phase screen. (a) The experimental setup, where the target is placed 1.5 m away from the imaging system. (b) The reconstruction of a USAF resolution target. (c) Magnified regions of various bar groups in (b). (d) Contrast plots for the reconstructed images under the three conditions. (e) Experimental results of the text part on a five-yuan RMB banknote; from left to right: low-resolution raw image, FP reconstruction with turbulence, TRMFP reconstruction, and FP reconstruction without turbulence.

Group 2 Element 4 (turbulence-free) to Group 1 Element 1 on the USAF target—a three-fold reduction in spatial resolution. This result highlights the limitation of single-frame FP under turbulence and underscores the need for dedicated turbulence mitigation. The third one is TRMFP reconstruction. TRMFP restores the maximum resolvable feature to Group 2 Element 2 on the USAF target—a two-fold improvement over the turbulence-corrupted result. Quantitatively, this corresponds to an angular resolution enhancement from 1.75×10^{-4} to 8.75×10^{-5} rad, approaching 80% of the turbulence-free performance. The robustness of TRMFP is also evident in the line profile comparison and magnified line pairs [Fig. 6(c)], where conventional FP exhibits significant blurring and distortion, while ours presents a stable reconstruction and approaches the ideal case.

Again, we use the contrast metric C [Eq. (15)] to evaluate the resolution performance. The area of white and black bars is manually located. Figure 6(d) plots the contrast metric for reconstructed images under the three conditions. We set a contrast threshold at 0.1 to determine the limit resolution of the reconstructed images, since the contrast value is around 0.1 for the Rayleigh criteria ($C = (1 - 0.81)/(1 + 0.81) \approx 0.1$). Therefore, the minimum resolvable bar group is (1,1) for FP with turbulence and (2,1) for TRMFP, which is basically consistent with the visual results in Fig. 6(b).

Table 1. Details of the Experimental Setup

Parameter	Phase Screens	Dynamic Turbulence
Imaging distance	1.5 m	5 m
Wavelength	639 nm	639 nm
Focal length	50 mm	75 mm
F-number	8	5.6
Aperture diameter	6.25 mm	13.39 mm
Pixel size	2.4 μm	2.4 μm
Number of positions	121	121
Step size	1.5 mm	1.5 mm
Synthetic aperture	21.35 mm	27.39 mm
Frame per position	20	20
Exposure time	80 ms	10 ms
Exposure gain	0	24 dB

In the second experiment, we use a five-yuan RMB as the target. Unlike the binary intensity profile of the USAF resolution test chart, the banknote exhibits continuous grayscale variations and

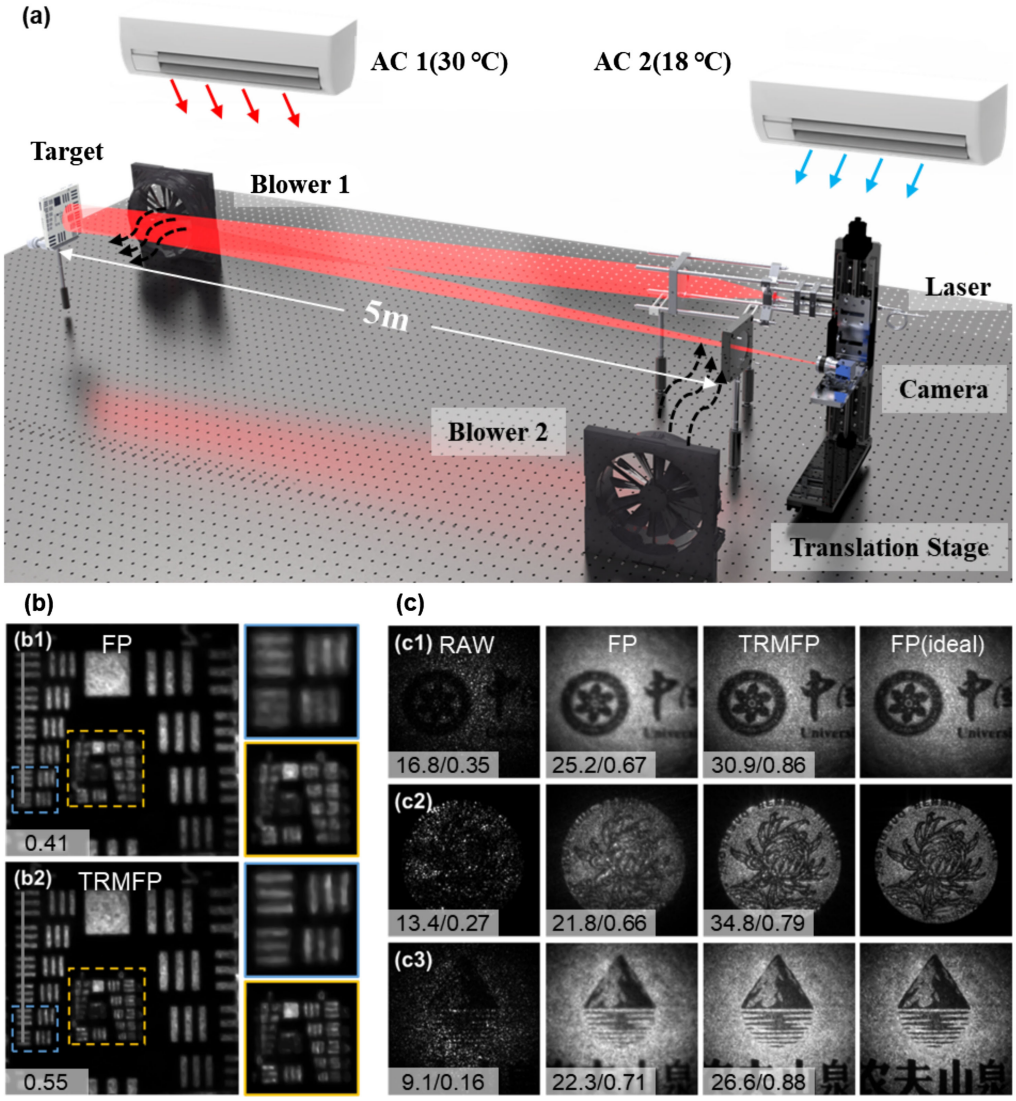

Fig. 7. TRMFP validation using laboratory-generated dynamic turbulence. (a) The experimental setup. (b) Experimental results of a USAF resolution target under dynamic turbulence: (b1) FP reconstruction, and (b2) TRMFP reconstruction, with contrast values of the line trace indicated in the lower-left corners. (c) Imaging performance across diverse materials under dynamic turbulence. From left to right: a single sub-aperture image, reconstruction using conventional FP under turbulent conditions, reconstruction using the proposed TRMFP method, and FP reconstruction under an ideal, turbulence-free condition, serving as a reference. Rows from top to bottom: (c1) canvas bag, (c2) coin, and (c3) plastic label. PSNR/SSIM values comparing each result with the ideal FP reconstruction are provided in the lower-left corners of (c1)–(c3).

stronger phase scattering effects, leading to significantly reduced image contrast and more pronounced speckle noise, as shown in Fig. 6(e). The image contrast within the magnified region for FP, TRMFP, and ideal FP is 0.2247, 0.2857, and 0.3727, respectively. These results demonstrate TRMFP's effectiveness: the turbulence-free reconstruction clearly resolves all text elements with high fidelity; turbulence-degraded FP reconstruction fails to distinguish the second and third text lines due to severe phase distortions; while the TRMFP reconstruction successfully restores text legibility, achieving performance comparable to the turbulence-free case.

B. Validation with Dynamic Turbulence

To validate the performance of TRMFP under spatiotemporally complex turbulence, we conducted a series of experiments under laboratory-generated dynamic turbulence conditions, as shown in Fig. 7(a). The imaging distance is extended to 5 m, and turbulence is induced using two complementary methods designed to produce strong convective refractive index variations along the optical path. The detailed experimental configuration, which leverages controlled temperature gradients and forced airflow, is provided in Appendix D, and key parameters are summarized in Table 1. Notably, the exposure time is set to 10 ms to meet the short-exposure condition and effectively "freeze" the turbulence. With $N = 20$ frames captured per scanning position and a total of 121 positions, the active acquisition time is approximately $121 \times 20 \times 0.01 = 24.2$ s, plus stage movement overhead. This multi-frame acquisition strategy, while increasing data volume, is essential for statistical turbulence suppression and remains practically manageable.

The performance of TRMFP is first evaluated using a USAF resolution target. The spatiotemporal nature of the wavefront distortions is visually confirmed by a sequence of raw frames provided

in the supplementary material (Visualization 1). As presented in Fig. 7(b), the reconstruction results demonstrate a substantial performance gap. Visually, TRMFP produces a significantly sharper image, which is quantitatively confirmed by the contrast values of the line trace. This is also quantitatively confirmed by the limiting resolution: conventional FP reconstruction only resolves features up to Group −1, Element 6, whereas TRMFP successfully resolves up to Group 0, Element 4, corresponding to a resolution improvement of approximately 1.6×. This clear improvement in resolvable spatial frequency validates the method's efficacy in mitigating spatiotemporal distortions.

To further demonstrate the practical applicability of TRMFP, we tested it on objects with diverse surface textures under the same dynamic turbulence conditions. Samples with varying surface roughness and reflectivity, including a coin, a canvas bag, and a plastic label, are selected to assess generalization performance. As shown in Fig. 7(c), TRMFP consistently recovers high-resolution images and effectively suppresses turbulence-induced distortions across all materials. Quantitative comparisons with the ideal turbulence-free FP reconstruction [PSNR/SSIM values provided in the lower-left corners of Figs. 7(c1)–7(c3)] further confirm the fidelity. These results confirm that the effectiveness of TRMFP is generalizable and not limited to specific object types or surface characteristics.

5. CONCLUSION

In summary, we have demonstrated turbulence-resilient macroscopic Fourier ptychography (TRMFP), a two-stage, closed-loop framework that unifies speckle-interferometry-based turbulence correction with joint ptychographic reconstruction and residual-aberration optimization to enable high-resolution imaging through strong optical turbulence. The key conceptual advance of TRMFP lies in reformulating Fourier ptychography as a statistically consistent inverse problem in random media, thereby bridging speckle interferometry and ptychographic synthetic aperture imaging within a unified framework. This approach recovers diffraction-limited sub-aperture images from turbulence-distorted measurements, enabling successful FP reconstruction under non-idealized conditions where conventional FP fails. Comprehensive validation—including numerical analysis, 1.5 m proof-of-principle experiments, and 5 m dynamic turbulence tests with diverse objects—confirms the method's effectiveness and robustness. The results show that, while maintaining computational complexity comparable to conventional FP, TRMFP recovers up to 80% of the turbulence-free resolution fidelity in our tests using a resolution target and achieves a two-fold resolution improvement over conventional FP under turbulence.

Notably, TRMFP achieves these gains without optical hardware modifications—requiring only a multi-frame short-exposure acquisition strategy. When compared to other turbulence compensation techniques, TRMFP offers a unique set of advantages. Unlike adaptive optics [44], it requires no complex wavefront sensing or corrective optics, providing a purely computational solution. In contrast to phase diversity [28], TRMFP does not rely on parameterized phase models or introduced defocus, making it more adaptable to dynamic, unknown turbulence conditions. While deep-learning methods (such as TurbNet [45] and TMT [46]) demand extensive training datasets and substantial computational resources, TRMFP is training-free, computationally affordable, and based on physical principles, ensuring interpretability and generalizability. Regarding computational cost, TRMFP introduces additional preprocessing and optimization steps, resulting in approximately $2-3\times$ longer reconstruction time compared to conventional FP in our unoptimized CPU implementation (Intel i5-9300H, 2.4 GHz). This overhead can be substantially reduced through parallelization and GPU acceleration and is well justified given that TRMFP enables high-resolution imaging under strong turbulence where conventional FP fails entirely. These attributes position TRMFP as a hardware-simple, computationally efficient alternative that balances performance with practical deployability.

It is important to note, however, that the current TRMFP framework operates under the isoplanatic assumption, where the PSF is considered the same across the field of view. This assumption holds for relatively small fields of view within the isoplanatic angle. In scenarios involving wide-field imaging or strong turbulence with significant anisoplanatism, the PSF may vary spatially, challenging the current model. Addressing such non-isoplanatic conditions remains an important direction for future work; a natural extension would be to incorporate field-dependent pupil functions, modeling the turbulence as a set of isoplanatic patches.

Overall, this work establishes a new paradigm for turbulence-resilient imaging through a pioneering fusion of speckle interferometry with closed-loop Fourier ptychography. This approach is distinguished by three key innovations: it is the first to apply the principles of speckle interferometry to FP for super-resolution; it introduces a residual-aberration correction method that jointly optimizes the object and the residual aberrations; and it provides the first FP-compatible solution for dynamic turbulence, surpassing static aberration correction approaches. Looking ahead, scaling this technology to practical long-range applications will require addressing specific challenges, including signal-to-noise ratio (SNR) degradation, increased turbulence severity, and longer acquisition times. The SNR degradation can be mitigated by the method's intrinsic reliance on statistical averaging, which suppresses uncorrelated noise. Acquisition time can be controlled through increasing the gain or hardware upgrades such as higher-power laser sources, cameras with superior sensitivity. Increased turbulence severity, characterized by a reduced Fried parameter, may be tackled by exploring synergies with adaptive optics (AO). AO can provide real-time correction of low-order aberrations, reducing the dynamic range required from TRMFP, while TRMFP handles fine-scale residual errors. A hybrid system could enable robust imaging under even stronger turbulence. Besides, while TRMFP is currently a purely physics-based method, incorporating data-driven priors could further enhance performance—for example, using deep learning to learn turbulence-invariant features or provide better initial guesses for optimization, while maintaining the interpretability of the physical model. With its turbulence-resilient super-resolution capability, this approach shows strong potential for applications in free-space optical communication, astronomical imaging, and remote sensing, where turbulence has long been a fundamental limitation.

APPENDIX A: ATMOSPHERIC TURBULENCE STATISTICS

The atmospheric turbulence can be described by the classical Kolmogorov turbulence model [47]. Within the inertial range ($l_0 \ll r \ll L_0$), the refractive index structure function takes the form:

$$D_n(r) = C_n^2 \cdot r^{2/3},\ l_0 \ll r \ll L_0, \tag{A1}$$

where l_0 and L_0 are the inner and outer scale of turbulence, respectively; and C_n^2 denotes the refractive index structure constant. Based on the Kolmogorov model, several key statistics can be derived as weighted integrals of C_n^2.

The first is the atmospheric coherence diameter, or Fried parameter (r_0) [32], given by

$$r_0 = [0.423k^2 \int_0^L C_n^2(z)\mathrm{d}z]^{-3/5}, \tag{A2}$$

where $k = 2\pi/\lambda$ is the wavenumber, and λ is the wavelength. Note that this is for plane wave propagation, where $z = 0$ is at the source and $z = L$ is at the camera. The Fried parameter defines the resolution limit of an imaging system viewing through turbulence: the achievable angular resolution is proportional to λ/r_0, rather than λ/D, where D is the diameter of the system aperture. Thus, turbulence strength is commonly quantified by the ratio D/r_0; a smaller r_0 indicates stronger turbulence.

The second parameter is the atmospheric coherence time (t_0) [48], representing the time over which the turbulent phase screen remains approximately stationary. It is related to the Fried parameter and the transverse wind velocity v by

$$t_0 \approx 0.314\frac{r_0}{v} = [2.91k^2 \int_0^L C_n^2(z)|v|^{5/3}\mathrm{d}z]^{-3/5}. \tag{A3}$$

Under typical atmospheric conditions, t_0 ranges from milliseconds to tens of milliseconds. An exposure time shorter than t_0 is considered "short exposure," effectively freezing the turbulence and resulting in an optical transfer function (OTF) with a wider passband, albeit with random phase fluctuations. Long exposures, in contrast, produce a smoother but bandwidth-limited OTF due to turbulence averaging.

The third parameter is the isoplanatic angle (θ_0) [49], which defines the angular region over which wavefront distortions remain correlated:

$$\theta_0 = [2.91k^2 \int_0^L C_n^2(z)z^{5/3}\mathrm{d}z]^{-3/5}. \tag{A4}$$

Within an angle smaller than θ_0, the PSF can be considered spatially invariant. This allows turbulence to be modeled as an isoplanatic degradation within the limited field of view.

APPENDIX B: PHASE SCREEN METHOD BASED ON ZERNIKE POLYNOMIAL

The phase-screen method based on Zernike polynomial is a widely used numerical approach to simulate the effect of turbulence, in which random phases are produced over the pupil and the atmospheric correlation is introduced with proper filtering by the Kolmogorov spectrum. The phase screen is represented by a linear combination of a series of Zernike polynomial [30]:

$$\phi = \sum_{j=1}^{\infty} a_j Z_j, \tag{B1}$$

where the phase screen is represented by ϕ, Z_j is the jth order Zernike polynomial, and a_j is the Zernike coefficient which is obtained by calculating its covariance matrix due to its atmospheric correlation. For a detailed explanation, the reader can refer to Noll's work [30], here we directly give the expression of (i, j) element of the covariance matrix when $i - j = 2k$ (when $i - j = 2k + 1$, $< a_i a_j >= 0$):

$$< a_i a_j >= 0.15(D/r_0)^{\frac{5}{3}} \cdot \frac{(-1)^{\frac{n_i+n_j-2m_i}{2}}[(n_i+1)(n_j+1)]^{1/2}\Gamma\left(\frac{14}{3}\right)\Gamma\left[(n_i+n_j-\frac{5}{3})/2\right]\delta_z}{\Gamma\left(\frac{n_i-n_j+17/3}{2}\right)\Gamma\left(\frac{n_j-n_i+17/3}{2}\right)\Gamma\left(\frac{n_i+n_j+23/3}{2}\right)}, \tag{B2}$$

where n_i, n_j, m_i, and m_j are the Noll coefficients corresponding to the ith and jth orders of Zernike polynomials, D is the aperture size, r_0 is the coherence length, and δ_z is the logical Kronecker symbol. Then, singular value decomposition is applied to the covariance matrix, and the coefficient a_j can be calculated by introducing Gaussian random variables b according to its eigenvector U:

$$a_j = \sum_{k=1}^{\infty} U_{jk} b_j. \tag{B3}$$

The phase screen is then obtained by adding together Zernike polynomials of each mode according to Eq. (B1). Finally, the resultant pupil function $P(\boldsymbol{u})$ is given by

$$P(\boldsymbol{u}) = \mathrm{circ}\left(k_0 \cdot \frac{1}{2F\#}\right)\exp(-j\phi), \tag{B4}$$

where circ$(\cdot)$ denotes a circular mask with a radius of $k_0 \cdot \frac{1}{2F\#}$, with k_0 representing the wave number and $F\#$ representing the F-number. Notably, various turbulence conditions can be simulated by adjusting the order of Zernike polynomials and the value of D/r_0 in Eq. (B2). In this work, we use the first 15 orders of Zernike polynomials to generate the phase screen. The whole process is summarized as follows:

1. In each camera position, randomly generate N phase screens $\phi_n, n = 1, 2, \ldots, N$, according to the above process, where N is the number of short-exposure images.
2. Calculate the corresponding turbulence-distorted pupil function $P_n(\boldsymbol{u})$ according to Eq. (B4).
3. Obtain the N turbulence-distorted images according to Eq. (1).
4. Repeat the above process for all camera positions.

APPENDIX C: EVALUATION INDEX

We use the structural similarity index (SSIM) and the Pearson correlation coefficient (PCC) to verify the performance of our method throughout the paper. The expressions are as follows:

$$\mathrm{SSIM}(O, G) = \frac{(2\mu_O\mu_G + C_1)(2\sigma_{OG} + C_2)}{(\mu_O^2 + \mu_G^2 + C_1)(\sigma_O^2 + \sigma_G^2 + C_2)}, \tag{C1}$$

$$\mathrm{PCC}(O, G) = \frac{\sum_{i=1}^{m}\sum_{j=1}^{n}(O(i,j)-\tilde{O})(G(i,j)-\tilde{G})}{\sqrt{\sum_{i=1}^{m}\sum_{j=1}^{n}(O(i,j)-\tilde{O})^2}\sqrt{\sum_{i=1}^{m}\sum_{j=1}^{n}(G(i,j)-\tilde{G})^2}}, \quad \text{(C2)}$$

where m and n are the width and height of the image. O denotes the reconstructed image, and G denotes the ground -truth. $\tilde{O}$ and $\tilde{G}$ are the mean value of the reconstructed image and ground -truth, respectively. μ_O is the mean of O, σ_O^2 and σ_{OG} are the variance of O and the covariance of O and G, respectively. $C_1 = (0.01L)^2$, $C_2 = (0.03L)^2$, where L is the dynamic range of the image.

APPENDIX D: LABORATORY-GENERATED DYNAMIC TURBULENCE

Here, we describe the setup for generating dynamic, convective turbulence in our laboratory environment. The setup is designed to create stochastic refractive index variations along the imaging path to test the TRMFP method under conditions more complex than static phase screens. As shown in Fig. 7(a), first, large-scale convective flow is induced by operating two laboratory air conditioning (AC) units at opposite ends of the room with a significant temperature differential (one set at 30°C and the other at 18°C), creating a stable gradient and continuous air mixing. Second, more intense and localized turbulence is generated by placing two electric blowers to blow hot air across the optical path, one near the object and another near the camera. This combination produced strong, spatiotemporally dynamic wavefront distortions. A video sequence of the resulting dynamic image distortions captured by the camera is provided as supplementary material (Visualization 2), visually demonstrating the spatiotemporal distortion.

Funding. Sichuan Science and Technology Program (2026NSFSC1443, 2023YFSY0059); National Natural Science Foundation of China (62175243).

Acknowledgment. J. Zhang thanks Dr. Di You for the helpful discussion on experimental preparation and data collection, and Dr. Yanda Gu and Dr. Yingben Song for their assistance in experimental data collection.

Disclosures. The authors declare no conflicts of interest.

Data availability. Data underlying the results presented in this paper are not publicly available at this time but may be obtained from the authors upon reasonable request.

REFERENCES

1. Q. Liu, Y. Di, M. Zhang, *et al.*, "Research progress on atmospheric turbulence perception and correction based on adaptive optics and deep learning," Adv. Photonics Res. **6**, 2400204 (2025).
2. N. J. Miller, M. P. Dierking, and B. D. Duncan, "Optical sparse aperture imaging," Appl. Opt. **46**, 5933–5943 (2007).
3. J. Dou and H. Dong, "A high-contrast imaging coronagraph for segmented-mirror large aperture telescopes using a spatial light modulator," Astron. Tech. Instrum. **1**, 166–170 (2024).
4. A. Moreira, P. Prats-Iraola, M. Younis, *et al.*, "A tutorial on synthetic aperture radar," IEEE Geosci. Remote Sens. Mag. **1**(1), 6–43 (2013).
5. M. Ryle, A. Hewish, and J. Shakeshaft, "The synthesis of large radio telescopes by the use of radio interferometers," IRE Trans. Antennas Propag. **7**, 120–124 (1960).
6. Z. Xie, K. Yang, Y. Liu, *et al.*, "1.5-m flat imaging system aligned and phased in real time," Photonics Res. **11**, 1339–1353 (2023).
7. K. Yang, X. Ma, W. Wei, *et al.*, "Model-driven extended scene piston sensing for synthetic aperture telescopes," Opt. Express **32**, 42071–42090 (2024).
8. J. Wang, Z. Jin, Y. Dai, *et al.*, "Calibration of a multiwavelength co-phase measurement system for a segmented solar telescope," Astron. Tech. Instrum. **2**, 1–11 (2025).
9. G. Zheng, R. Horstmeyer, and C. Yang, "Wide-field, high-resolution Fourier ptychographic microscopy," Nat. Photonics **7**, 739–745 (2013).
10. G. Zheng, C. Shen, S. Jiang, *et al.*, "Concept, implementations and applications of Fourier ptychography," Nat. Rev. Phys. **3**, 207–223 (2021).
11. X. Ou, R. Horstmeyer, C. Yang, *et al.*, "Quantitative phase imaging via Fourier ptychographic microscopy," Opt. Lett. **38**, 4845–4848 (2013).
12. S. Dong, P. Nanda, R. Shiradkar, *et al.*, "High-resolution fluorescence imaging via pattern-illuminated Fourier ptychography," Opt. Express **22**, 20856–20870 (2014).
13. T. Nguyen, Y. Xue, Y. Li, *et al.*, "Deep learning approach for Fourier ptychography microscopy," Opt. Express **26**, 26470–26484 (2018).
14. P. Song, S. Jiang, T. Wang, *et al.*, "Synthetic aperture ptychography: coded sensor translation for joint spatial-Fourier bandwidth expansion," Photonics Res. **10**, 1624–1632 (2022).
15. H. Zhou, B. Y. Feng, H. Guo, *et al.*, "Fourier ptychographic microscopy image stack reconstruction using implicit neural representations," Optica **10**, 1679–1687 (2023).
16. X. Wu, N. Zhou, Y. Chen, *et al.*, "Lens-free on-chip 3D microscopy based on wavelength-scanning Fourier ptychographic diffraction tomography," Light Sci. Appl. **13**, 237 (2024).
17. Q. Zhao, R. Wang, S. Zhang, *et al.*, "Deep-ultraviolet Fourier ptychography (DUV-FP) for label-free biochemical imaging via feature-domain optimization," APL Photonics **9**, 090801 (2024).
18. J. Zhang, W. Wei, K. Yang, *et al.*, "Toward robust super-resolution imaging: a low-rank approximation approach for pattern-illuminated Fourier ptychography," APL Photonics **9**, 066106 (2024).
19. S. Dong, R. Horstmeyer, R. Shiradkar, *et al.*, "Aperture-scanning Fourier ptychography for 3D refocusing and super-resolution macroscopic imaging," Opt. Express **22**, 13586–13599 (2014).
20. J. Holloway, M. S. Asif, M. K. Sharma, *et al.*, "Toward long-distance subdiffraction imaging using coherent camera arrays," IEEE Trans. Comput. Imaging **2**, 251–265 (2016).
21. J. Holloway, Y. Wu, M. K. Sharma, *et al.*, "SAVI: synthetic apertures for long-range, subdiffraction-limited visible imaging using Fourier ptychography," Sci. Adv. **3**, e1602564 (2017).
22. S. Li, B. Wang, K. Liang, *et al.*, "Far-field synthetic aperture imaging via Fourier ptychography with quasi-plane wave illumination," Adv. Photonics Res. **4**, 2300180 (2023).
23. Q. Zhang, Y. Lu, Y. Guo, *et al.*, "200 mm optical synthetic aperture imaging over 120 meters distance via macroscopic Fourier ptychography," Opt. Express **32**, 44252–44264 (2024).
24. Z. Tian, M. Zhao, D. Yang, *et al.*, "Optical remote imaging via Fourier ptychography," Photonics Res. **11**, 2072–2083 (2023).
25. B. Wang, S. Li, Q. Chen, *et al.*, "Learning-based single-shot long-range synthetic aperture Fourier ptychographic imaging with a camera array," Opt. Lett. **48**, 263–266 (2023).
26. S. Li, B. Wang, H. Guan, *et al.*, "Snapshot macroscopic Fourier ptychography: far-field synthetic aperture imaging via illumination multiplexing and camera array acquisition," Adv. Imaging **1**, 011005 (2024).
27. M. Xiang, A. Pan, Y. Zhao, *et al.*, "Coherent synthetic aperture imaging for visible remote sensing via reflective Fourier ptychography," Opt. Lett. **46**, 29–32 (2021).
28. M. Xiang, A. Pan, J. Liu, *et al.*, "Phase diversity-based Fourier ptychography for varying aberration correction," Front. Phys. **10**, 848943 (2022).
29. S. Li, B. Wang, H. Guan, *et al.*, "Inverse synthetic aperture macroscopic Fourier ptychographic imaging of moving targets," Laser Photonics Rev. e02758 (2026), early posting.
30. R. J. Noll, "Zernike polynomials and atmospheric turbulence*," J. Opt. Soc. Am. **66**, 207–211 (1976).
31. C. M. Harding, R. A. Johnston, and R. G. Lane, "Fast simulation of a Kolmogorov phase screen," Appl. Opt. **38**, 2161–2170 (1999).
32. D. L. Fried, "Optical resolution through a randomly inhomogeneous medium for very long and very short exposures," J. Opt. Soc. Am. **56**, 1372–1379 (1966).
33. D. Liu, H. Liu, Z. Jin, *et al.*, "High accuracy deep learning wavefront sensing under high-order turbulence," Astron. Tech. Instrum. **1**, 316–324 (2024).
34. R. G. Paxman, B. J. Thelen, and J. H. Seldin, "Phase-diversity correction of turbulence-induced space-variant blur," Opt. Lett. **19**, 1231–1233 (1994).
35. A. Labeyrie, "Attainment of diffraction limited resolution in large telescopes by Fourier analysing speckle patterns in star images," Astron. Astrophys. **6**, 85 (1970).

36. C. Denker, G. Yang, and H. Wang, "Near real-time image reconstruction," Sol. Phys. **202**, 63–70 (2001).
37. J. Davis and W. Tango, "Measurement of the atmospheric coherence time," Publ. Astron. Soc. Pac. **108**, 456 (1996).
38. A. Kellerer and A. Tokovinin, "Atmospheric coherence times in interferometry: definition and measurement," Astron. Astrophys. **461**, 775–781 (2007).
39. B. Hwang, T. Woo, C. Ahn, *et al.*, "Imaging through random media using coherent averaging," Laser Photonics Rev. **17**, 2200673 (2023).
40. X. Ou, G. Zheng, and C. Yang, "Embedded pupil function recovery for Fourier ptychographic microscopy," Opt. Express **22**, 4960–4972 (2014).
41. A. Beck and M. Teboulle, "Fast gradient-based algorithms for constrained total variation image denoising and deblurring problems," IEEE Trans. Image Process. **18**, 2419–2434 (2009).
42. M. Odstrcil, P. Baksh, S. A. Boden, *et al.*, "Ptychographic coherent diffractive imaging with orthogonal probe relaxation," Opt. Express **24**, 8360–8369 (2016).
43. W. Eschen, L. Loetgering, V. Schuster, *et al.*, "Material-specific high-resolution table-top extreme ultraviolet microscopy," Light Sci. Appl. **11**, 117 (2022).
44. Y. Guo, L. Zhong, L. Min, *et al.*, "Adaptive optics based on machine learning: a review," Opto-Electron. Adv. **5**, 200082 (2022).
45. Z. Mao, A. Jaiswal, Z. Wang, *et al.*, "Single frame atmospheric turbulence mitigation: a benchmark study and a new physics-inspired transformer model," in *Computer Vision – ECCV*, S. Avidan, G. Brostow, M. Cissé, *et al.*, eds. (Springer Nature, 2022), pp. 430–446.
46. X. Zhang, Z. Mao, N. Chimitt, *et al.*, "Imaging through the atmosphere using turbulence mitigation transformer," IEEE Trans. Comput. Imaging **10**, 115–128 (2024).
47. A. N. Kolmogorov, "The local structure of turbulence in incompressible viscous fluid for very large Reynolds numbers," Proc. Math. Phys. Sci. **434**, 9–13 (1991).
48. M. Panahi, R. Shomali, M. Mollabashi, *et al.*, "Atmospheric coherence time measurement by four-aperture DIMM defocus velocity technique," Appl. Opt. **58**, 8673–8679 (2019).
49. L.-K. Yu, Z.-H. Hou, S.-C. Zhang, *et al.*, "Isoplanatic angle in finite distance: experimental validation," Opt. Eng. **54**, 024105 (2015).